



HAL
open science

Machine learning and registration for automatic seed localization in 3D US images for prostate brachytherapy

Hatem Younes, Jocelyne Troccaz, Sandrine Voros

► To cite this version:

Hatem Younes, Jocelyne Troccaz, Sandrine Voros. Machine learning and registration for automatic seed localization in 3D US images for prostate brachytherapy. *Medical Physics*, 2021, 48 (3), pp.1144-1156. 10.1002/mp.14628 . hal-03023560

HAL Id: hal-03023560

<https://hal.science/hal-03023560v1>

Submitted on 25 Nov 2020

HAL is a multi-disciplinary open access archive for the deposit and dissemination of scientific research documents, whether they are published or not. The documents may come from teaching and research institutions in France or abroad, or from public or private research centers.

L'archive ouverte pluridisciplinaire **HAL**, est destinée au dépôt et à la diffusion de documents scientifiques de niveau recherche, publiés ou non, émanant des établissements d'enseignement et de recherche français ou étrangers, des laboratoires publics ou privés.

Machine learning and registration for automatic seed localization in 3D US images for prostate brachytherapy

Hatem YOUNES¹, Jocelyne TROCCAZ¹ and Sandrine VOROS^{1,2}

¹ Univ. Grenoble Alpes, CNRS, TIMC-IMAG, F-38000 Grenoble, France

² Grenoble INP,INSERM, F-38000 Grenoble, France

{Hatem.Younes; Sandrine.Voros; Jocelyne.Troccaz}@univ-grenoble-alpes.fr

Abstract

Purpose: New radiation therapy protocols, in particular adaptive, focal or boost brachytherapy treatments, require determining precisely the position and orientation of the implanted radioactive seeds from real-time ultrasound (US) images. This is necessary to compare them to the planned one and to adjust automatically the dosimetric plan accordingly for next seeds implantations. The image modality, the small size of the seeds and the artifacts they produce make it a very challenging problem. The objective of the presented work is to set-up and to evaluate a robust and automatic method for seed localization in 3D US images.

Methods: The presented method is based on a pre-localization of the needles through which the seeds are injected in the prostate. This pre-localization allows focusing the search on a region of interest (ROI) around the needle tip. Seeds localization starts by binarizing the ROI and removing false positives using respectively a Bayesian classifier and a Support Vector Machine (SVM). This is followed by a registration stage using first an Iterative Closest Point (ICP) for localizing the connected set of seeds (named strand) inserted through a needle, and secondly refining each seed position using Sum of Squared Differences (SSD) as a similarity criterion. ICP registers a geometric model of the strand to the candidate voxels whilst SSD compares an appearance model of a single seed to a subset of the image. The method was evaluated both for 3D images of an Agar-agar phantom and a dataset of clinical 3D images. It was tested on stranded and on loose seeds.

Results: Results on phantom and clinical images were compared with a manual localization giving mean errors of 1.09 ± 0.61 mm on phantom image and 1.44 ± 0.45 mm on clinical images. On clinical images, the mean errors of individual seeds orientation was $4.33 \pm 8.51^\circ$.

Conclusions: The proposed algorithm for radioactive seed localization is robust, tested on different US images, accurate, giving small mean error values, and returns the 5 cylindrical seeds degrees of freedom.

Keywords: Prostate brachytherapy, Radioactive seed localization , 3D Ultrasound image, Bayesian classifier, support vector machine (SVM), iterative closest point (ICP), Sum of squared Differences (SSD)

40 Contents

41	I. Introduction	1
42	I.A. State of the art	2
43	II. Materials and Methods	5
44	II.A. Needle detection	5
45	II.B. Seeds localization	6
46	II.B.1. Thresholding: Binary Bayesian classifier	6
47	II.B.2. False positive voxels removal: Support Vector Machine (SVM)	7
48	II.B.3. Global stranded seeds localization	9
49	II.B.4. Improvement of individual seeds localization	9
50	II.C. Materials	10
51	II.C.1. Phantom experiments	10
52	II.C.2. Clinical experiments	11
53	III. Results	11
54	III.A. Phantom image	11
55	III.A.1. Global strand localization	11
56	III.A.2. Pose refinement	12
57	III.B. Clinical images	13
58	IV. Discussion	13
59	V. Conclusion	16
60	VI. Acknowledgments	16
61	References	17
62	VII. Figures	23

63 I. Introduction

64 Prostate cancer is the 3rd most frequently diagnosed cancer in men worldwide, accounting
65 for 1.27 million new cases in 2018 ¹. Brachytherapy ² using low dose rate radioactive seeds
66 is an effective treatment for low risk prostate cancer. It aims at delivering a specific and
67 homogeneous radiation dose to the prostate whilst limiting the dose delivered to organs at
68 risk (urethra, rectum and bladder). This requires a planning step determining the number
69 and optimal positions of seeds from pre-operative images: most often transrectal US images.
70 In a typical brachytherapy procedure ¹ parallel needles are inserted into the patient's prostate
71 through the skin of the perineum with the help of a guiding grid named template. Once
72 the needle tip reaches the wanted position, the seeds are released through the needle. Two
73 strategies are possible depending on the type of seeds: stranded seeds are pre-assembled
74 with spacers using connectors and released as a whole for each insertion direction. On the
75 opposite, loose seeds are released one by one, which makes needle retraction more complex
76 and progressive. Needle insertion and seed implantation are performed under the control of
77 transrectal US imaging (generally reconstructed in 3D from translated axial 2D US).

78 In practice, seed implantation is performed manually with some imprecision which re-
79 sults from operator variable expertise, prostate motion and deformation, edema, needle
80 deflection, etc. Stranded seeds reduce delivery inaccuracy and seed migration compared to
81 loose seeds. However, in both cases, the brachytherapy procedure may require a planning
82 update, at some stage, taking into account the real position of already implanted seeds.
83 Detecting them most often requires human intervention. In this paper we propose a novel
84 method for automatic seeds localization in 3D US images. Connected to a fast replanning ³,
85 this allows to envision a fully automatic adaptive brachytherapy, that is an intra-operative
86 update of the seeds placement planning, based on the localization and actual dosimetry map
87 of the previously implanted seeds.

88 Detecting the seeds is a challenging task due to their small volume (cylinder: $\emptyset=0.8$
89 mm and 5 mm in length for I^{125} seeds) and to the low quality of the US imaging modality.

¹<https://www.mayoclinic.org/tests-procedures/prostate-brachytherapy/multimedia/permanent-prostate-brachytherapy/img-20008710>

I.A. State of the art

90
91 The accurate localization of seeds is an active field of research. Several approaches have
92 been proposed operating on various image modalities, like magnetic resonance (MRI), X-ray
93 images (computed tomography CT or fluoroscopy) and ultrasound images (US). Because of
94 its excellent soft-tissue contrast, MRI is essentially used for diagnostic. It could be also used
95 for seed localization post-operatively: Kuo et al. ^{MRI} developed an algorithm based on the blob
96 detection technique using the Laplacian of a Gaussian (LoG). Generally the CT images are
97 used to perform post-implant dosimetry one month after seeds implantation. In this context,
98 N’Guyen et al. ^{CTseedSegmentation} proposed an approach to determine seeds position and orientation in CT
99 images using K-means and principal component analysis (PCA) techniques; the method
100 allows to separate seeds grouped in clusters, a situation that may occur with loose seeds.
101 MRI only and CT-MRI fusion-based works are proposed to localize seeds post-operatively
102 using Deep Neural Network (DNN) methods for low-dose-rate prostate brachytherapy ^{nosrati2019postin}.
103 Whilst CT and MRI may be exploited for pre-operative diagnostic or planning or post-
104 operative assessment, they cannot be used for intra-operative control of seed position. A
105 possible intra-operative solution is to obtain the real position from X-ray images acquired
106 with a C-arm as presented in ^{Xray}. However the prostate is not visible in X-ray images. US
107 imaging is thus the effective modality used today to guide brachytherapy as it acquires real-
108 times images, which is particularly relevant in the context of moving and deformable soft
109 tissue.

110 In this section we describe some of the few methods proposed in the literature to localize
111 seeds in US images. Because seeds are injected through needles, some seed localization
112 methods start with the needle tip localization. This allows building a ROI to be explored.

113 Wei et al. ^{SeedLocalization1} proposed a workflow composed of 6 iterative instructions. First steps aim
114 to detect the needle, build the ROI and threshold the obtained volume. Then, neighboring
115 candidate voxels, potentially corresponding to seeds, are grouped into clusters. Seeds are
116 localized by detecting the center and the orientation of each cluster using the PCA method.
117 Finally, clusters which dimensions do not correspond to seed dimensions are removed. These
118 steps are repeated until all implanted seeds have been localized. The method was tested
119 on Agar-agar and chicken phantoms with a CT-based ground truth. Such a method may
120 only be used to localize loose seeds since strands dimensions vary with their composition.

121 As pointed by the authors, selecting the threshold may be very challenging since US images
122 vary a lot from patient to patient.

123 In a rather similar way, Wen et al. ^{SeedLocalizationNeedle2} detect seeds by computing a ROI using the
124 preoperative dosimetry plan, thresholding using the Otsu method ^{Otsu}, clustering the voxels
125 and pruning the set of clusters using dimension information. Needle track based on Hough
126 Transform (HT) is used a posteriori to filter the seed detection results. The method was
127 evaluated on a commercial tissue equivalent phantom. However, the information deduced
128 from the preoperative dosimetry plan may be inaccurate to construct the ROI. Indeed, as the
129 inserted needle may deviate from the target, seeds may be released away from the planned
130 positions. The challenges of real clinical images are also underlined by the authors.

131 Based on a DNN, Holupka et al. ^{DNN} determine the position of the seeds from two
132 dimensional transaxial transrectal US clinical images. A common DNN, called DetectNet
133 was trained using 950 US images and tested on 90 validation US images. The network
134 was trained from a data base of 2D clinical images manually segmented. The results on 10
135 patients were compared with the corresponding positions in CT images to obtain an average
136 error of 2.29 mm. However, CT images were acquired one to three months after the day
137 of the implant where prostate gland may inflate causing seeds positions displacement. To
138 compensate this, obtained seeds positions were transformed according to an empirical scaling
139 factor representing the prostate shape change.

140 Deep learning was also used by Golshan et al. ^{golshan2020automatic}. The same type of engineered neural
141 network (CNN) was applied to locate the needle and its implanted stranded seeds. The
142 learning phase is based on rather small number of 3D images of anonymous patients: 13
143 images containing 238 seeds. It was carried out with patches, which are 3D cubic sub-
144 regions of the ultrasound images, representing models for a 'seed' region and of a 'non seed'
145 region. Localization results were compared with an expert manual localization on ultrasound
146 images giving $F1_score = 0,7$ (seed considered as true positive when its localization error is
147 smaller than 2.5 mm).

148 Dehghan et al. recently proposed a solution ^{EMenhanced} for seed detection based on electromag-
149 netic (EM) needle tracking, which allowed recording of seed dropping locations. A 3D US
150 volume was obtained after each injection. Then, successive registered volumes were sub-
151 tracted to obtain a difference volume. There, seed candidates were detected using their

152 extended reverberations as a signature. Finally, false positive seeds were removed by com-
 153 paring their locations with the expected location which corresponds to the seed dropping
 154 locations. However, the transfer to clinical routine of EM tracking (and associated needle
 155 modification) is not straightforward.

156 Table [I](#) summarizes the [tab_state_of_the_art](#) presented methods. Most of them do not allow for a fully
 157 automatic binarization. Methods also differ regarding the number of localization parameters
 158 that are determined. Ideally, the complete pose of a cylindrical seed requires 5 parameters
 159 $(x, y, z, \theta_x, \theta_y)$. Given the cylindrical shape of the seed, θ_z is meaningless and an arbitrary
 160 value can be chosen. Many methods consider only the position of the seed (3 parameters)
 161 and this may be sufficient when dose calculation relies on very simple 1D model (the seed is
 162 considered as a point source and the delivered dose is spherical). However, since very long
 163 [rivard2004update](#), the American Association of Physicists in Medicine (AAPM) recommends the use of 2D
 164 dose models for cylindrical seeds. Taking full benefit of such models requires knowing the
 165 orientation of the seed. Collins Fekete et al. [collins2014quantifying](#) showed on patient data that orientations
 166 errors may have in impact on the dose delivered to organs at risks. Moreover adaptive
 167 brachytherapy involves more complex dose models [inversePlanning](#) requiring a full localization of the seed.
 168 Finally, published methods differ in their level of evaluation. Whilst, all the methods cited in
 169 table [I](#) compare to CT based ground truth, most of them are limited to phantom experiments.
 170 Only the deep learning-based methods present results on real patient images.

171 In this paper, we aim at determining the 5 pose parameters of stranded seeds. An initial
 172 stage consists in localizing the needle before seed insertion to reduce the ROI to the relevant
 173 region (see § [II.A.](#)). In order to [sec:Needledetection](#) adapt to local variations in the image and to the patient, we
 174 propose an automatic thresholding method based on Bayesian classification (see § [II.B.1.](#) [sec:Bayesian](#)).
 175 False positive voxels, that may be selected by thresholding, then detected and removed using
 176 SVM classifier (§ [II.B.2.](#) [False_positive_removal](#)). As presented in § [II.B.3.](#) [sec:ICP](#), binary images are first processed using
 177 planning information to localize stranded seeds in the ROI as a whole. In a second stage
 178 explained in section [II.B.4.](#) [sec:orientations](#), individual seeds are precisely localized by locally comparing the
 179 grey level of the original image to a seed 3D US image template. The approach was evaluated
 180 on two experimental setups: a phantom experiment allowed us to compare our localization
 181 method of dummy seeds in an Agar-agar phantom to a a reference manual segmentation
 182 (§ [II.C.1.](#) [sec:phantom_experiments](#)). The method was also tested on routine clinical images and also compared to a
 183 reference manual segmentation (§ [II.C.2.](#) [sec:clinical_experiments](#)). The associated results are presented in section

[sec:Phantomseedlocalizationresults](#)
[III.A.](#) and [III.B.](#).

II. Materials and Methods

Seeds localization begins with a needle detection which is an essential step to build the ROI where seeds are released. First, we introduce the employed method to localize a needle in 3D US images which we previously developed. Then we explain the seed localization method modeled by the workflow of Fig. [fig:workflow](#) 1.

II.A. Needle detection

Needle detection is done using the previous work [ourWork](#) [16](#) based on binary Bayesian classification. We proposed a method to localize needle in 3D US images. Needle voxels within US volumes are brighter than the other voxels, and form a voxel class selected according to the Bayesian classifier:

$$\pi_{X_n} P(I(x) = y | X_n) \underset{X_b}{\geq} \pi_{X_b} P(I(x) = y | X_b) \quad (1)$$

- X_n = needle voxel class.
- X_b = background (non-needle) voxel class.
- $y = I(x)$ = voxel intensity x .
- π_{X_i} = prior probabilities.
- $P(I(x) = y | X_i)$ = Gaussian probabilities.

Where: a voxel x is classified in X_n if the posterior probability of X_n is larger than that of X_b . The way parameters of the probabilistic model are estimated and a curve representing the needle is fitted to data is fully explained in [ourWork](#) [16](#). The proposed method was successfully tested on anonymized 3D US clinical images. Fig. [fig:needles_lolalized](#) 2 shows a typical result example. In order to obtain a good estimate of the dropping location of seeds, with respect to the previous work [ourWork](#) [16](#), we added a new step to refine the needle tip search along the detected curve. The tip is the last voxel along the curve where

$$P(X_n | I(x)) \leq P(X_b | I(x)) \quad (2)$$

BayesianTip

209 As shown in Fig. [3](#), the detection is successful even for a needle passing through a shadow
 210 region, which is a dark region that corresponds to some reflected signals attenuation. Needle
 211 detection allows to build the ROI where seeds are supposed to be located. As shown in
 212 Fig. [4](#), the ROI is a parallelepipedic frame which dimensions depend on the length of the
 213 released strand supposed to be inside. As explained in § [II.B.3](#) and shown in table [2](#), strands
 214 compositions and lengths are recoverable from the treatment planning. The next subsection
 215 describes the method for seeds localization in the ROI.

216 II.B. Seeds localization

217 The current proposed method has been designed for stranded seeds localization. The work-
 218 flow shown in Fig. [1](#) contains the main steps and methods used to detect and localize
 219 oriented seeds. We detail each step separately in the following subsections. The first typical
 220 step for object detection is to separate it from the background.

221 II.B.1. Thresholding: Binary Bayesian classifier

222 A thresholding step aims to separate seeds voxels from background. The classical method
 223 consists in defining a threshold value τ and classifying as follows:

$$Seeds = \{x : I(x) \geq \tau\}$$

224

$$Background = \{x : I(x) < \tau\}$$

225 Because of the presence of high intensity artifacts and the high variability of grey levels in
 226 US images, defining thresholds for binarization is very challenging. This is why we propose
 227 to use a Bayesian classifier to perform binarization without a static threshold definition. In
 228 a way similar to needle detection, seeds and background voxels are described through two
 229 separated peaks which can be modeled using an additive Gaussian Mixture Model (GMM).
 230 The Bayesian classifier [17](#) assigns the most likely class to a given observed feature which is
 231 the voxel intensity.

$$232 \quad C_{Bayes}(y) = \underset{X_i}{\operatorname{argmax}} \quad P(Cl = X_i \mid I(x) = y) \quad (3) \quad \text{eq:Bayes1}$$

233 Where $Cl = \{X_s(\text{Seeds}), X_b(\text{Background})\}$,
 234 and $I(x) = y$ is the voxel intensity. According to Bayes theorem:

$$235 \quad P(Cl = X_i | I(x) = y) = \frac{\pi_{X_i} P(I(x) = y | Cl = X_i)}{P(I(x) = y)} \quad (4) \quad \boxed{\text{eq:Bayes2}}$$

236 Where π_{X_i} are the prior probabilities and $P(I(x) = y | X_i)$ are the Gaussian probabilities.
 237 The intensities $I(x)$ are independent within each class, which justifies the Bayes theorem
 238 application. According to equations (5) and (4), naive Bayesian classifier assigns to each
 239 voxel the class which maximizes $\underset{X_i}{\operatorname{argmax}} \left\{ \frac{\pi_{X_s} P(I(x)=y | Cl=X_s)}{P(I(x)=y)}, \frac{\pi_{X_b} P(I(x)=y | Cl=X_b)}{P(I(x)=y)} \right\}$. Finally,
 240 binary Bayesian classification to be used is summarized as inequalities (5): ineq:Bayes1

$$241 \quad \pi_{X_s} P(I(x) = y | X_s) \underset{X_b}{\geq} \pi_{X_b} P(I(x) = y | X_b) \quad (5) \quad \boxed{\text{ineq:Bayes1}}$$

242 Several parameters are required: $\{\pi_{X_i}, \mu_i, \sigma_i\}$ where $i = \{s, b\}$ and μ, σ are the Gaussian
 243 parameters. These parameters vary from one stranded seed to another even in the same
 244 image. According to a criterion of maximum likelihood, parameters are predicted by ap-
 245 proaching as much as possible the distribution of seeds volume histogram. This is done via
 246 with the well known Expectation-Maximization algorithm (EM algorithm ^{EM}₁₅). EM is applied
 247 on a Gaussian mixture model to estimate the unknown parameters by an iterative process,
 248 which computes the maximum-likelihood of a given vector of features for each iteration. EM
 249 algorithm iterates parameters calculation until their convergence. Fig. fig:firstTwoSteps
 250 example.

251 II.B.2. False positive voxels removal: Support Vector Machine (SVM)

ve_removal

252 It naturally happens that some background voxels are assigned as seed voxels. In order
 253 to remove these false positives, we propose to apply an additional discriminator: Support
 254 Vector Machine (SVM), a learning classifier. In the case of binary classification, a SVM
 255 maximizes the margin between classes C^1 of false positive voxels and C^2 of true positive
 256 voxels ($C^1 \cup C^2 = X_s$). It aims to find the hyperplane that separates classes optimally. In
 257 the linear case, the main equation to establish the hyperplane equation is:

$$258 \quad h(x) = w^T x + w_0 \quad (6)$$

259 where $x = (x_1, \dots, x_N)$ is the input vector which contains voxel features, w is the normal
 260 vector to the hyperplane and w_0 is the offset of the hyperplane from the origin along the

261 normal vector w . Finally the last parameters (w^T and w_0) determine the classifier as follows:

262

263

$$x \mapsto \text{sign}(w^T \cdot x + w_0) \quad (7)$$

264 The input vector x is assigned to the appropriate class regarding to the sign of $(w^T \cdot x + w_0)$.

265 It represents the position of x with respect to the hyperplane. As mentioned previously, the

266 input vector x represents the input voxel to be classified. It contains the voxel features. Clas-

267 sification results depend on the selected features. Based on the specificity of brachytherapy

268 application, we propose to use two gradient-based features: indeed, stranded seeds injection

269 in the prostate follows the \vec{Z} axis of the 3D US image, so the intensity change of seeds

270 voxels according to \vec{X} and \vec{Y} could have high value, contrarily to others outliers voxels

271 (Fig. [fig:firstTwoSteps](#)). The gradient magnitude ($|G_x|, |G_y|$) along \vec{X} and \vec{Y} provide a good discriminative

272 representation as shown in Fig. [fig:hyperplane](#) where $x = (x_1, x_2) = (G_x, G_y)$, $\{G_x, G_y\}$ are the gradi-

273 ent magnitudes. The gradient magnitudes are computed from the original US image. The

274 Sequential Minimal Optimization (SMO [\[15\]](#)) algorithm is used to compute the hyperplane

275 equation parameters (w^T, w_0) . It transforms the problem of parameters prediction into the

276 dual problem:

$$277 \quad h(x) = w^T x + w_0 = \sum_{i=1}^N \alpha_i y^{(i)} \langle x^{(i)}, x \rangle + w_0 \quad (8)$$

278 where

279 • $(x^{(i)}, y^{(i)}) =$ training data.

280 • $y^{(i)} = \{-1 \text{ if } x^{(i)} \in C^1, 1 \text{ if } x^{(i)} \in C^2\}$.

281 • $\alpha \in \mathfrak{R}^N =$ Lagrange multipliers.

282 • $N =$ the training data length.

283 For training the SVM, we chose three ROI containing different stranded seeds compositions

284 and different artifacts locations for which we calculated and labelled the features ($|G_x|, |G_y|$).

285 SMO was trained on the fusion of these three datasets to return the best separative hyper-

286 plane which maximizes the distance at the nearest data point of each group. A typical SVM

287 discrimination result is shown in Fig. [fig:firstTwoSteps](#).

II.B.3. Global stranded seeds localization

288
sec:ICP

289 At this stage, strand voxels have been computed using a succession of two classifiers. As
 290 proposed in the workflow (of Fig. [fig:workflow](#) [1](#)), the next step aims at localizing each strand considered
 291 as a whole within selected voxels. This is done by rigidly registering a geometric model of
 292 the stranded seeds to the seed voxels detected in the previous steps, represented by their cen-
 293 ters. This is performed using the Iterative Closest Point (ICP) algorithm [\[26\]](#). One objective
 294 is to transform the 3D voxels already selected into a set of connected cylinders. A second
 295 very important objective is to distinguish seeds from spacers connecting them since their US
 296 appearance is very similar (Fig. [5](#) (a)). Based on the treatment planning, we construct the
 297 model of the strand injected through each needle. This model, which is a set of 3D surface
 298 points, describes the succession of cylinders that represent radioactive seeds linked through
 299 spacers. Fig. [7](#) shows two real strands and their corresponding models. We propose to
 300 employ ICP to superimpose the two sets of 3D points. ICP requires a suitable initialization
 301 of the relative position of data to be rigidly registered. Since the closest known position of
 302 the strand to be localized is the needle tip, the model is initialized at needle tip coordinates
 303 (obtained as specified in [sec:NeedleDetection](#) [II.A.](#)) and is aligned with the insertion direction. It allows to find
 304 the optimal transformation representing the location of the strand as a whole:

$$305 \quad T_{Strand} = \{\theta_x^{Strand}, \theta_y^{Strand}, t_x^{Strand}, t_y^{Strand}, t_z^{Strand}\}, \quad \text{where} \quad \{\theta_x^{Strand}, \theta_y^{Strand}\}$$

306 and $\{t_x^{Strand}, t_y^{Strand}, t_z^{Strand}\}$ are respectively the rotations and the translations applied on
 307 the strand relatively to the ROI frame $\{\vec{X}, \vec{Y}, \vec{Z}\}$ (Fig. [4](#)). Given the cylindrical shape of
 308 the strands, it is impossible to determine the rotation around its \vec{Z} axis. This information
 309 is meaningless and an arbitrary value can be given.

II.B.4. Improvement of individual seeds localization

310
orientations

311 After the ICP convergence, the optimal position of the strand model with respect to the
 312 binary image information is obtained, where all seeds are well aligned. However, in practice,
 313 stranded seeds may not remain straight, as the linkers may break during the insertion. It
 314 may result in subsets of linked seeds with different orientations as shown in Fig. [5](#). As seeds
 315 mislocations may modify the delivered dose, an additional stage is necessary and consists
 316 in refining each seed pose separately. From that stage, spacers are no longer considered.
 317 Knowing precisely the pose of each seed would allow to update the dosimetry and replan,

when necessary, the positions of the next seeds to be injected. This refinement is an image-based rigid registration comparing an appearance model of a seed V_m to a subset V_s of the real gray level image. V_s is computed from the location of the strand obtained in [II.B.3.](#) V_m was obtained by selecting a clearly visible seed in an image among those of our dataset (Fig. [fig:VS](#)). This appearance model was applied for all localized seeds.

$$T_{seed} = \underset{T}{argmin} \sum_{x,y,z} (V_m(x, y, z) - T(V_s(x, y, z)))^2 \quad (9)$$

The optimal transformation T_{seed} is the one that minimizes the sum of squared differences (SSD) value between the model volume V_m and the seed volume V_s moved according to T where $T = \{\theta_x^{Seed}, \theta_y^{Seed}, t_x^{Seed}, t_y^{Seed}\}$. Similarly to the strand, θ_z^{Seed} cannot be determined and is meaningless. Moreover, because seeds, connectors and spacers have similar response and appear as a whole in the $\overrightarrow{Z_{Strand}}$ direction (Fig. [fig:phantom-seed](#)), refining $\overrightarrow{Z_{Strand}}$ is impracticable. This is why neither t_z^{Seed} nor θ_z^{Seed} are considered at this stage. θ_z^{Seed} can be arbitrarily chosen and t_z^{Seed} value is kept similar to what was computed in the previous stage.

II.C. Materials

The approach was tested both on phantom image and on clinical images. This section describes the data acquisition and validation protocol for both types of experiments.

II.C.1. Phantom experiments

Using a proportion of 2.8% of Agar-agar contained in a plastic box (Fig. [fig:KOELIS_Trinity_workstation](#)), we constructed a phantom sufficiently rigid to avoid any movement of released seeds. We created a preoperative dosimetry plan where 8 needles were inserted. Each of them was used to release one strand. The strands composition is given in table [tab_Stranded_seeds_compositions](#). The phantom with the implanted seeds was scanned using the 3D side-fire ultrasound probe of the TRINITY[®] (Koelis, Meylan, France) assistance workstation for prostate interventions shown in Fig. [fig:KOELIS_Trinity_workstation](#). 3D images were produced using the probe internal motor moving a linear array transducer on 170° around the probe axis. The center frequency of the transducer was set to 7 MHz, and the capturing depth was set to 80 mm. The size of generated images was 95x95x80 mm, with a voxel size of 0.3125x0.3125x0.3125 mm. Seeds in the phantom image are as shown in Fig. [fig:phantom-seed](#).

345 To measure the error of the presented seed localization method, we compared automatic
346 localization with a manual segmentation considered as a ground truth. We evaluated the
347 precision of the manual segmentation by repeating it at 7 distant times, and obtained a
348 standard deviation of 0.66 mm.

349 II.C.2. Clinical experiments

350 The algorithm was also tested on anonymized 3D US images of two patients. Each patient's
351 prostate with the implanted seeds was scanned using a biplane endocavity Z848 TRUS probe
352 within the Medical Flex Focus 500 ultrasound workstation. Its biplane transducer acquired
353 75 axial images of resolution 600x580 and a 3D image was reconstructed with a voxel size
354 of 0.26x0.26x1 mm. The evaluation was also done by comparing the automatic localization
355 with a manual segmentation considered as a ground truth. Because of the very low quality
356 of the images (Fig. [fig:firstTwoSteps](#) 5), we had to select a few strands for which a manual segmentation could
357 be reliably done. 4 stranded seeds were selected from the data of patient 1 containing in total
358 11 seeds. For the image of patient 2, 3 stranded seeds containing 6 seeds were processed.
359 Detailed compositions of stranded seeds are presented in table [tab_Statistics](#) 3. We have first measured the
360 variability of the manual segmentation by repeatedly segmenting the centers of three seeds
361 in the two images, at 7 distant times. The obtained standard deviation was 0.7 mm.

362 III. Results

363 After describing the results of our method using the phantom validation protocol, we present
364 the corresponding results on 3D US clinical images. The parameters values used for each US
365 image type are summarized in table [tab:parameters](#) 4.

366 III.A. Phantom image

367 III.A.1. Global strand localization

368 The errors on the seed localization are computed as the Euclidean distances between the
369 centers of the automatically detected and manual identified seeds. Fig. [fig:boxplotPhantom](#) 12 presents the
370 statistics of these errors before (3.08 ± 1.55 mm) and after (1.55 ± 0.80 mm) global strands

371 localization where the unknowns are $(t_x^{Strand}, t_y^{Strand}, t_z^{Strand}, \theta_x^{Strand}, \theta_y^{Strand})$. The errors be-
 372 fore global strands localization correspond to the distance between the seeds of the strand
 373 model initialized at the needle tip and the ground-truth positions.

374 III.A.2. Pose refinement

sec:pose

375 As described in section §[11.B.4.](#), [sec:orientations](#) pose refinement relies on a second rigid registration based
 376 this time on voxel intensity differences. Fig. [fig:boxplotPhantom](#) 12 gives the corresponding boxplot before and
 377 after seed pose refinement where the unknowns are (t_x^{Seed}, t_y^{Seed}) (more details in figure S-
 378 1). The global error is measured as the Euclidean distance between the seeds centers. The
 379 mean error is 1.09 ± 0.61 mm. It was not possible to refine the orientations of individual
 380 seeds implanted in the phantom because strands did not break, and the strand remained
 381 perfectly straight. Therefore, we tested pose refinement on phantom data only for t_x^{Strand} ,
 382 t_y^{Strand} . We simulated orientation errors by rotating the seed volume V_s and studied how
 383 well the transformation parameters could be recovered. Seeds of a strand do not deviate a
 384 lot compared to loose seeds. Their deviations are mainly between -20° and $+20^\circ$ relative
 385 to a direction according to an orientation effects study on the post-planning dosimetry of
 386 low-dose-rate prostate brachytherapy [collins2014quantifying](#) 16. Therefore tests were performed between -20° and
 387 $+20^\circ$. Based on the template grid dimensions where needle holes are located every 5 mm in
 388 \vec{X} and \vec{Y} , a natural dimension in \vec{X} and \vec{Y} of $V_{s/m}$ would not exceed $\sim 2 \times 5$ mm to ensure
 389 that $V_{s/m}$ contain only one seed. The only constraint along \vec{Z} is the seed length. Taking into
 390 account the linker, we chose 6 mm as the 3rd dimension of $V_{s/m}$. Given the voxels resolution,
 391 we ended with $V_{s/m}$ dimensions of 11.25x10.31x9 mm. The seed appearance within V_m is
 392 shown in Fig. [fig:orientations](#) 13. The results of the simulation obtained on two seeds are presented in Fig.
 393 [fig:orientations](#) 13 left column (rotation around \vec{X}_{Strand}) and middle column (rotation around \vec{Y}_{Strand}). Each
 394 row corresponds to a seed where the red curve contains the applied angles and the blue curve
 395 contains the estimated values. As shown in Fig. [fig:VS](#) 8, seed and artifact signal are merged in
 396 the transversal plane, contrarily to the sagittal one where the seed is clearly visible. As a
 397 rotation around \vec{Y}_{Strand} corresponds to a motion in the transversal plane, this rotation angle
 398 cannot be accurately refined by our method because of the artifacts, as illustrated by Fig.
 399 [fig:orientations](#) 13, middle column. Although the information exists, the estimation of the seed orientations
 400 around \vec{Y}_{Strand} failed with the chosen dimensions of $V_{s/m}$: indeed those dimensions affect
 401 the orientations estimation, when they are of the same order of magnitude as the artifacts

402 dimensions. This was confirmed by extending the dimensions of V_s and V_m to 18.75x10.31x9
 403 mm (60x33x29 voxels) instead of 11.25x10.31x6 mm (36x33x19 voxels) and running the same
 404 experiments. The simulation results for the rotation around $\overrightarrow{Y_{Strand}}$ with this new $V_{s/m}$ size
 405 are shown in Fig. [fig:orientations](#), third column. The mean errors decrease from 7.4° and 19° to 2.55°
 406 and 2.44° . It can be concluded that the small cropping of V_s and V_m is problematic because
 407 of the artifact extending laterally over the volumes. This will be discussed in section [sec:discussion](#) [IV..](#)

408 III.B. Clinical images

cal images

409 Fig. [fig:boxplotpatients](#) [14](#) presents the localization errors before global strand localization (2.36 ± 1.11 mm),
 410 before (1.59 ± 0.55 mm) and after (1.44 ± 0.45 mm) individual seeds refinement (more
 411 details in figure S-2). The unknown parameters are $(t_x^{Seed}, t_y^{Seed}, \theta_x^{Seed})$. Table [tab-Statistics](#) [3](#) contains
 412 the seeds orientations refinement compared with the manual estimation. As explained in
 413 [§III.A.2.](#), it was impossible to refine the rotation around $\overrightarrow{Y_{Strand}}$ axis. Rotation could be
 414 taken into account to some extent if the US images were acquired during seed insertions, but
 415 here the US data was acquired post-operatively with all seeds implanted. We will discuss
 416 this point in [sec:discussion](#) [§IV..](#)

417 IV. Discussion

discussion

418 Challenges in seed localization from 3D US images are essentially due to the low quality
 419 of the imaging modality and the small seed volume. Thus, some echogenic structures can
 420 mimic seed appearance and some seeds brightness are affected when they are in a shadow
 421 region. In this paper we aimed to overcome these difficulties by introducing an automatic
 422 seed localization using different machine learning and rigid registration algorithms.

423 An accurate segmentation of candidate seeds voxels is mandatory for the localization of
 424 the seeds. To do so, we performed a thresholding using a Bayes classification, followed by a
 425 false-positives removal using an SVM. The EM algorithm of the Bayes classification converges
 426 to local optima, and therefore requires a careful initialization of the means and variances
 427 parameters. How this initialization is handled is fully described in [ourWork](#) [16](#). The same approach
 428 was used for seed localization to obtain the adequate initialization values summarized in
 429 table [tab:parameters](#) [4](#). The following SVM false-positives removal step is a refinement which could not

430 replace the Bayes Classification step. Indeed, SVM would then be applied to the original
 431 gray-level voxels, resulting in a huge amount of input points. This would be computationally
 432 expensive (estimation of the gradients of all the non-zero voxels of the US image). Moreover,
 433 this would reduce the precision of the estimation, as it would increase the number of points
 434 close to the hyperplane.

435 Regarding seeds localization, it has been shown in § [III.A.2](#)^{sec:pose} that the orientation around
 436 $\overrightarrow{Y_{Strand}}$ could not be refined by the image-based local registration because of the US artifacts
 437 and the small size of V_s and V_m . An incremental procedure would be a potential solution for
 438 extending the volumes of V_s and V_m . For the first released strands, it would be performed
 439 without overlaps. Then, taking into account the neighbor potential seeds already detected
 440 would allow to enlarge V_m . The incremental procedure could also allow to introduce priors
 441 on previously detected seeds to modify this last stage. Of course, this would need further
 442 developments and testing.

443 The presented method was evaluated using two different US acquisition devices, on two
 444 different types of data (phantom and clinical), resulting in quite different image contents
 445 and quality. Despite this variety, only a few of the different parameters used to establish the
 446 classification and registration models needed to be tuned: the initialization values for the
 447 parameters estimations of the Bayes classification using EM depend on the probe devices,
 448 as illustrated by table [4](#)^{tab:parameters}. Neither the SMO initialization values (false-positives removal
 449 using an SVM) nor the ICP initialization values (for the global strand registration) had
 450 to be adapted. SMO was trained using phantom data, but the estimated hyperplanes for
 451 phantom or clinical images are very close, despite the differences in image content, thanks
 452 to our choice of features. The only other device-dependent element is the seed appearance
 453 model V_m . We selected for each image type the most generic appearance model. Adapting
 454 the few device dependent parameters (EM initialization values and V_m model) to new US
 455 imaging devices would be quite straightforward although additional pre-clinical experiments
 456 would be needed.

457 Despite the different experimental conditions, such as the probe technologies which
 458 provide different US images types (2D or 3D), qualities and resolutions, we try to compare
 459 the current work with the state of the art. Clinical images are used only in the deep learning-
 460 based works ([11](#)^{DNN} and [12](#)^{golshan2020automatic}). Although very promising, supervised learning requires large amount

461 of precisely labeled clinical images to show good performance and ability to generalize: this
462 may be a big issue as testify the published papers. The seed locations are determined by
463 a commercial software in CT volume in [\[11\]](#)^{DNN} and by an expert manual identification on US
464 images in [golshan2019automatic](#). Obtained results are within 2.29 mm and 2.5 mm (used to calculate $F1_score$)
465 respectively in [\[11\]](#)^{DNN} and [golshan2020automatic](#). As for us, the mean errors for patients images are 1.52 mm for
466 the 1st patient and 1.36 mm for the 2nd one. These good results need to be confirmed
467 on larger clinical data. Concerning other mentioned methods, different types of phantom
468 images are used (summarized in table [I](#))^{tab_state_of_the_art}. Seeds localization in phantom images is more
469 accurate than that in a biological tissues images. For example, it is approximately 1.03 mm
470 using Agar-agar phantom and 1.66 mm in chicken phantom [\[8\]](#)^{SeedLocalization1}. As for us, obtained result on
471 Agar-agar phantom is about 1.09 mm. According to Su et al. [\[21\]](#)^{investigation}, a localization error less
472 than 2 mm is customarily considered to be acceptable. They investigated the effects of a
473 seed mislocation on the dosimetry accuracy and showed that an error of 2 mm accounts for
474 less than 5% deviation in the dose delivered to 90% of the prostate volume. Collins Fekete
475 et al. [collins2014quantifying](#)¹⁰ demonstrated that orientation errors may have an impact on the dose delivered
476 to organs at risks. Moreover, new focal treatments appear where a reduced number of
477 seeds are inserted in an hemi-gland or even more locally for instance for a boost secondary
478 treatment. Al-Qaisieh et al. [al2015dosimetry](#)²² stresses the importance of sophisticated dose models and
479 accurate localization of seeds for focal treatments. The presented method could contribute
480 to such longer term applications.

481 As mentioned before, the use of stranded seeds decreases the implantation errors since
482 it brings them together to make a single injection per needle. We tested the algorithm
483 on various strand compositions. N8 of the table [2](#)^{tab_Stranded_seeds_compositions} released a strand composed just by
484 one seed. Also, the composition of S1 of the table [3](#)^{tab_Statistics} is just one seed. It proves that this
485 method, contrarily to the state of the art methods, could be a solution for both stranded and
486 loose seeds localization. However if loose seeds are clustered the method would fail as the
487 other methods presented in § [I.A.](#)^{State_of_the_art}. This question was addressed by N'Guyen et al. for CT
488 images [CTseedSegmentation](#)⁹, and we could consider adapting their approach for the case of US images. Most
489 methods of table [I](#)^{tab_state_of_the_art} focused on loose seeds except the recent deep learning-based method
490 [golshan2020automatic](#)¹² which was tested on strands. Loose and stranded seeds localization are two different
491 problems considering the inability to differentiate between spacers and seeds which have
492 similar response and appearance in the US images.

493 The proposed workflow has been specifically designed for stranded seeds localization in
494 US images. It would probably not be directly applicable to other imaging modalities (MRI
495 or CT) but several components of the approach could be generalized to another modality.
496 Combining US information with other intra-operative data such as cone beam computed
497 tomography (CBCT) image could be envisioned but the benefit/complexity ratio has to be
498 carefully evaluated.

499 Regarding the clinical applicability of the presented method, several protocols can be
500 envisioned. In a first stage, the automatic localization could simply happen when the pe-
501 ripheral seeds have been injected. This would allow re-planning for central seeds. However,
502 ideally, the adaptive planning would be done much more often. In a way very similar to
503 robot-assisted brachytherapy ^{cunha2010}where the robot generally handles a single needle and re-
504 quires repeating needle insertion-seeds injection, re-planning could occur before each new
505 needle insertion.

506 V. Conclusion

507 Adaptive brachytherapy requires an intra-operative update of the seeds placements, for which
508 localizing the seeds is essential. We proposed an image-based solution for the localization
509 (position and orientation estimation) of stranded seeds, which could also be applied to loose
510 seeds. Our validation was performed both on phantom and clinical data, with two different
511 US imaging devices. Our results are encouraging as the position accuracy is in-par with
512 clinical requirements, and the orientation accuracy is improved compared to state of the art.
513 Improvements and more extensive evaluations on clinical images will be needed to further
514 validate the approach.

515 VI. Acknowledgments

516 We thank LATIM and Brest University hospital for giving access to patient images. This was
517 made possible through the clinical protocol FOCUS NCT03160365 "Innovative planning and
518 guidance system for focal prostate brachytherapy. This work was partly supported by the
519 French ANR within the Investissements dAvenir program (Labex CAMI ANR-11-LABX)

520 and through the FOCUS (ANR-16-CE19-0011) and MIAI@Grenoble_Alpes (ANR-19-P3IA-
521 0003) projects.

523 References

- 525 **World2018**¹ F. Bray, J. Ferlay, I. Soerjomataram, R. L. Siegel, L. A. Torre, and A. Jemal, Global
526 cancer statistics 2018: GLOBOCAN estimates of incidence and mortality worldwide for
36 cancers in 185 countries, *CA: a cancer journal for clinicians* **68**, 394–424 (2018).
- Brachytherapy**² H. Raziee, A. Berlin, P. Chung, J. Helou, H. Jiang, J. M. Crook, and C. N. Catton,
528 Permanent seed brachytherapy for low risk prostate cancer, long term outcome, and
529 urinary toxicity, *International Journal of Radiation Oncology Biology Physics* **99**, E262
530 (2017).
- Brachytherapy Planning**³ K. A. Mountris, D. Visvikis, and J. Bert, DVH-based inverse planning using Monte
532 Carlo dosimetry for LDR prostate brachytherapy, *International Journal of Radiation
533 Oncology* Biology* Physics* **103**, 503–510 (2019).
- MRI**⁴ N. Kuo, J. Lee, C. Tempany, M. Stuber, and J. Prince, MRI-based prostate brachyther-
535 apy seed localization, in 2010 IEEE International Symposium on Biomedical Imaging:
536 From Nano to Macro, pages 1397–1400, IEEE, (2010).
- Segmentation**⁵ H.-G. Nguyen, C. Fouard, and J. Troccaz, Segmentation, separation and pose estima-
538 tion of prostate brachytherapy seeds in CT images, *IEEE Transactions on Biomedical
539 Engineering* **62**, 2012–2024 (2015).
- Postimplant**⁶ R. Nosrati, M. Wronski, C. Tseng, H. Chung, A. Pejović-Milić, G. Morton, G. Staniszc,
541 Postimplant Dosimetry of Permanent Prostate Brachytherapy: Comparison of MRI-Only
542 and CT-MRI Fusion-Based Workflows, *International Journal of Radiation Oncology*
543 Biology* Physics* **106**, 206–215 (2019).
- Xray**⁷ C. A. di San Filippo, G. Fichtinger, W. J. Morris, S. E. Salcudean, E. Dehghan, and
545 P. Fallavollita, Intraoperative segmentation of iodine and palladium radioactive sources
546 in C-arm images, *International journal of computer assisted radiology and surgery* **9**,
547 769–776 (2014).

- 13
549
550
- 8 Z. Wei, L. Gardi, D. B. Downey, and A. Fenster, Automated localization of implanted seeds in 3D TRUS images used for prostate brachytherapy, *Medical physics* **33**, 2404–2417 (2006).
- onNeedle21
552
553
- 9 X. Wen, S. E. Salcudean, and P. D. Lawrence, Detection of brachytherapy seeds using 3-D transrectal ultrasound, *IEEE Transactions on Biomedical Engineering* **57**, 2467–2477 (2010).
- Otsu4
555
- 10 N. Otsu, A threshold selection method from gray-level histograms, *IEEE transactions on systems, man, and cybernetics* **9**, 62–66 (1979).
- DNN6
557
- 11 E. J. Holupka et al., The Detection of Implanted Radioactive Seeds On Ultrasound Images Using Convolution Neural Networks, (2018).
- Automatic8
559
560
- 12 M. Golshan, D. Karimi, S. Mahdavi, J. Lobo, M. Peacock, S. Salcudean, I. Spadinger, Automatic detection of brachytherapy seeds in 3D ultrasound images using a convolutional neural network, *Physics in Medicine & Biology* (2020).
- Enhanced1
562
563
- 13 E. Dehghan, S. Bharat, C. Kung, A. Bonillas, L. Beaulieu, J. Pouliot, and J. Kruecker, EM-enhanced US-based seed detection for prostate brachytherapy, *Medical physics* **45**, 2357–2368 (2018).
- 2004update4
565
566
- 14 M. Rivard, B. Coursey, L. DeWerd, W. Hanson, M. Saiful Huq, G. Ibbott, M. Mitch, R. Nath, J. Williamson, Update of AAPM Task Group No. 43 Report: A revised AAPM protocol for brachytherapy dose calculations, *Medical physics* **31**, 633–674 (2004).
- antifying7
568
569
- 15 C. Collins Fekete, M. Plamondon, A. Martin, É. Vigneault, F. Verhaegen, L. Beaulieu, Quantifying the effect of seed orientation in postplanning dosimetry of low-dose-rate prostate brachytherapy, *Medical physics* **41**, (2014).
- ourWork6
571
572
- 16 H. Younes, S. Voros, and J. Troccaz, Automatic needle localization in 3D ultrasound images for brachytherapy, in 2018 IEEE 15th International Symposium on Biomedical Imaging (ISBI 2018), pages 1203–1207, IEEE, (2018).
- bayes3
574
- 17 I. Rish et al., An empirical study of the naive Bayes classifier, in IJCAI 2001 workshop on empirical methods in artificial intelligence, volume 3, pages 41–46, (2001).
-

- EM**₅¹⁸ A. P. Dempster, N. M. Laird, and D. B. Rubin, Maximum likelihood from incomplete data via the EM algorithm, *Journal of the Royal Statistical Society: Series B (Methodological)* **39**, 1–22 (1977).
576
577
- SMG**₈¹⁹ Z.-Q. Zeng, H.-B. Yu, H.-R. Xu, Y.-Q. Xie, and J. Gao, Fast training support vector machines using parallel sequential minimal optimization, in 2008 3rd international conference on intelligent system and knowledge engineering, volume 1, pages 997–1001, IEEE, (2008).
579
580
581
- ICP**₂²⁰ D. Chetverikov, D. Svirko, D. Stepanov, and P. Krsek, The trimmed iterative closest point algorithm, in Object recognition supported by user interaction for service robots, volume 3, pages 545–548, IEEE, (2002).
583
584
- Investigation**₁₃²¹ Y. Su, B. J. Davis, K. M. Furutani, M. G. Herman, and R. A. Robb, Dosimetry accuracy as a function of seed localization uncertainty in permanent prostate brachytherapy: increased seed number correlates with less variability in prostate dosimetry, *Physics in Medicine and Biology* **52**, 3105 (2007).
586
587
588
- Dosimetry**₃₉²² B. Al-Qaisieh, J. Mason, P. Bownes, A. Henry, L. Dickinson, H. Ahmed, M. Emberton, S. Langley, Dosimetry modeling for focal low-dose-rate prostate brachytherapy, *International Journal of Radiation Oncology* Biology* Physics* **92**, 787–793 (2015).
590
591
- 2010toward**₂²³ J A. Cunha, I C. Hsu, J. Pouliot, M. Roach III, K. Shinohara, J. Kurhanewicz, G. Reed, D. Stoianovici, Toward adaptive stereotactic robotic brachytherapy for prostate cancer: demonstration of an adaptive workflow incorporating inverse planning and an MR stealth robot, *Minimally Invasive Therapy & Allied Technologies* **19**, 189–202 (2010).
593
594
595

Table 1: Comparative study about proposed methods for seeds localization.

tab_state_of_the_art

	Problem to solve	Methods	US images	Ground truth
Wei et al. SeedLocalization1	Loose seeds positions + orientations in 3D image	Gray Level Change GLC >T	Agar-agar phantom Chicken phantom	CT images
Wen et al. SeedLocalizationNeedle2	Loose seeds positions in 3D image	Otsu Otsu	Tissue-equivalent ultrasound prostate phantom model 053	CT/Fluoroscopic scan images
Holupka et al. DNN	Loose seeds positions in 2D image	Deep learning	Clinical	CT images
Golshan et al. golshan2020automatic	Stranded seeds positions in 3D image	Deep learning	Clinical	US images
Dehghan et al. EMenhanced	Loose seeds positions in 3D image	US seed detection enhanced by EM-seed track	Yezitronix phantom	CT images
This study	Loose and stranded seeds positions + orientations in 3D images	Machine learning and rigid registrations methods	Agar-agar phantom Clinical	Manual localization of the US images

Table 2: Compositions of stranded seeds released by the needles in the phantom.

tranded_seeds_compositions

Needle	Released stranded seeds composition
N1	Seed + Spacer + Seed
N2	2 x Seed + Spacer + Seed
N3	Seed + 2 x Spacer + Seed
N4	2 x (Seed + Spacer) + Seed
N5	3 x Seed
N6	2 x Seed + Spacer + Seed + 2 x Spacer + Seed
N7	2 x Seed + Spacer + 2 x Seed
N8	Seed

Table 3: Statistics of localization error on 3D US images of two patients and error of estimated orientations of seeds composing the strands S_i ; $i \in [1;4]$.

tab_Statistics

		Stranded seeds composition	Error of estimated orientation in degree		Localization error in mm	
			mean \pm std	[min;max]	mean \pm std	[min;max]
Patient 1	S1	Seed + Spacer + 3x Seed	12.5 \pm 17.03	[1;37]	1.52 \pm 0.64	[0.91;2.64]
	S2	2x Seed	0.5 \pm 0.7	[0;1]		
	S3	Seed + 2x Spacer+Seed	1.5 \pm 2.12	[0;3]		
	S4	2x Seed+ 3x Spacer+Seed	4.33 \pm 1.52	[3;6]		
Patient 2	S1	Seed	2 \pm 0	[2;2]	1.36 \pm 0.22	[1.2;1.82]
	S2	2x Seed+ 3x Spacer+Seed	1.33 \pm 1.52	[0;3]		
	S3	Seed+ 2x Spacer + Seed	1.5 \pm 0.7	[1;2]		

Table 4: Parameters values used for each image type acquired by two different US probes. The EM and SVM parameters are unitless.

tab:parameters

	EM Initialization						SVM		ICP
	$\mu_{X_{TG}}$	μ_{X_B}	$\sigma_{X_{TG}}$	σ_{X_B}	$\pi_{X_{TG}}$	π_{X_B}	C	tol	threshold ϵ_{ICP}
Phantom image	235	100	3	40	0.05	0.95	0.15	10 e-3	0.01 mm
Clinical images	255	80	8	40	0.2	0.8	0.15	10 e-3	0.01 mm

596 VII. Figures

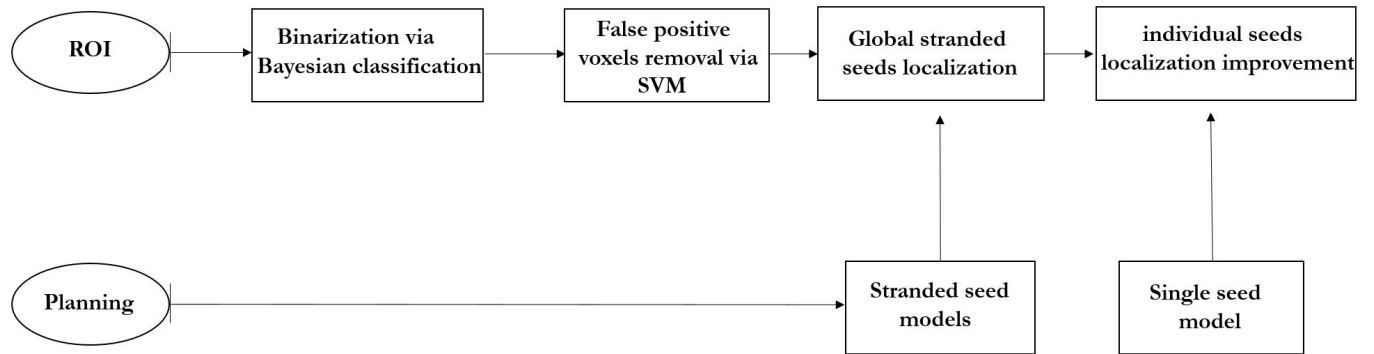


fig:workflow

Figure 1: Workflow for oriented seeds localization.

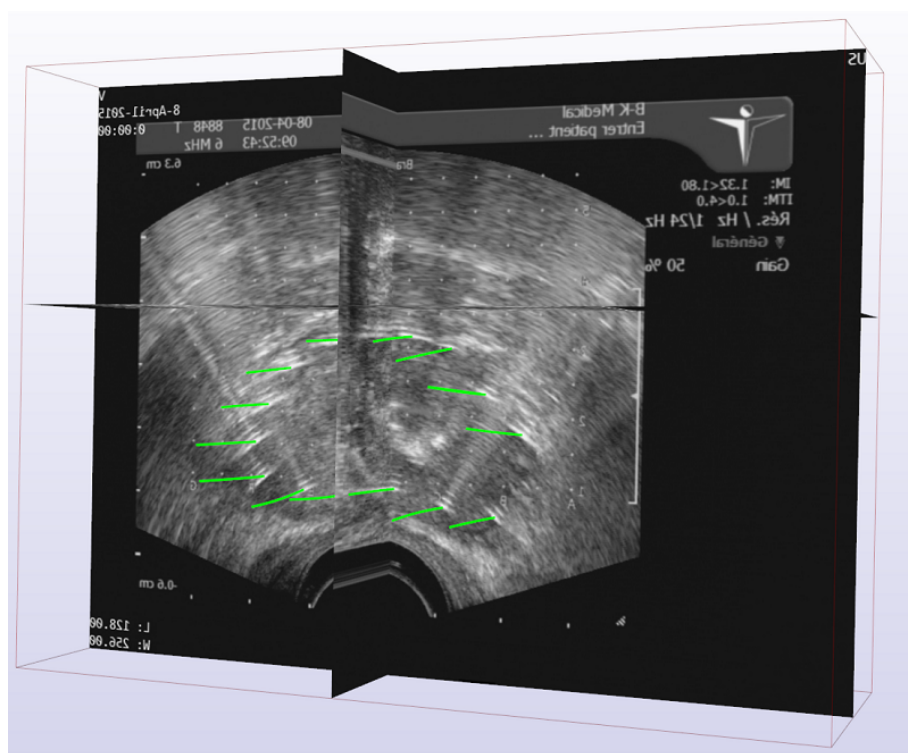


Figure 2: Detection of needles (green curves) in clinical images using needle detection method ^{ourwork} 16.

Fig:needles lolalized

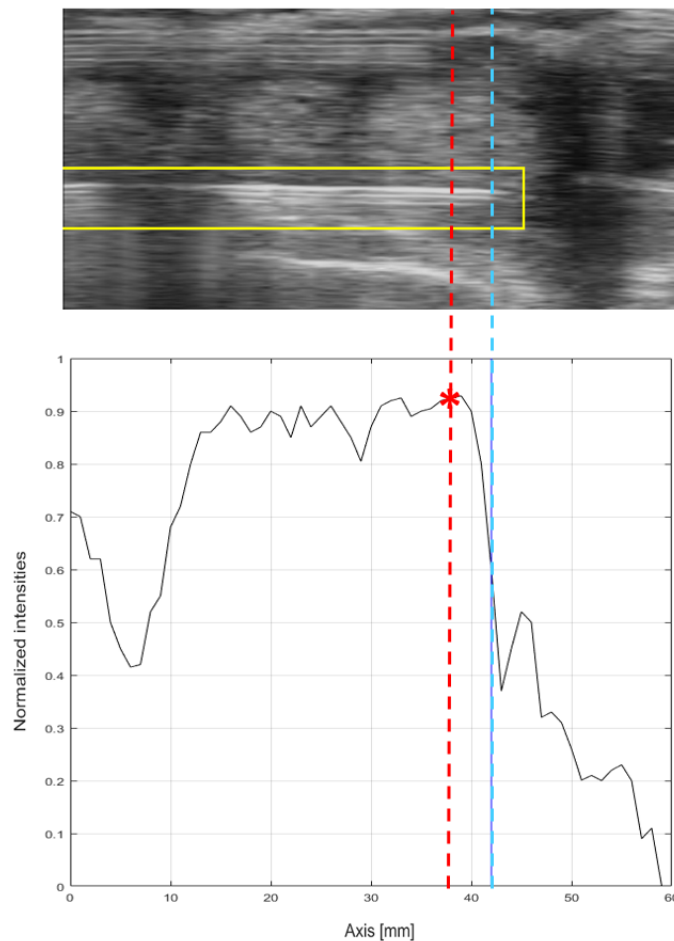


Figure 3: Needle tip localization example. Successful automatic localization despite a shadow region [3mm-15mm] where the needle's voxels intensities decrease significantly. The blue line corresponds to the first pixel of the needle shaft belonging to the background class (Bayes rule of inequality 2). The end of the needle initially detected is presented by the broken line passing through the red star.

fig:tip

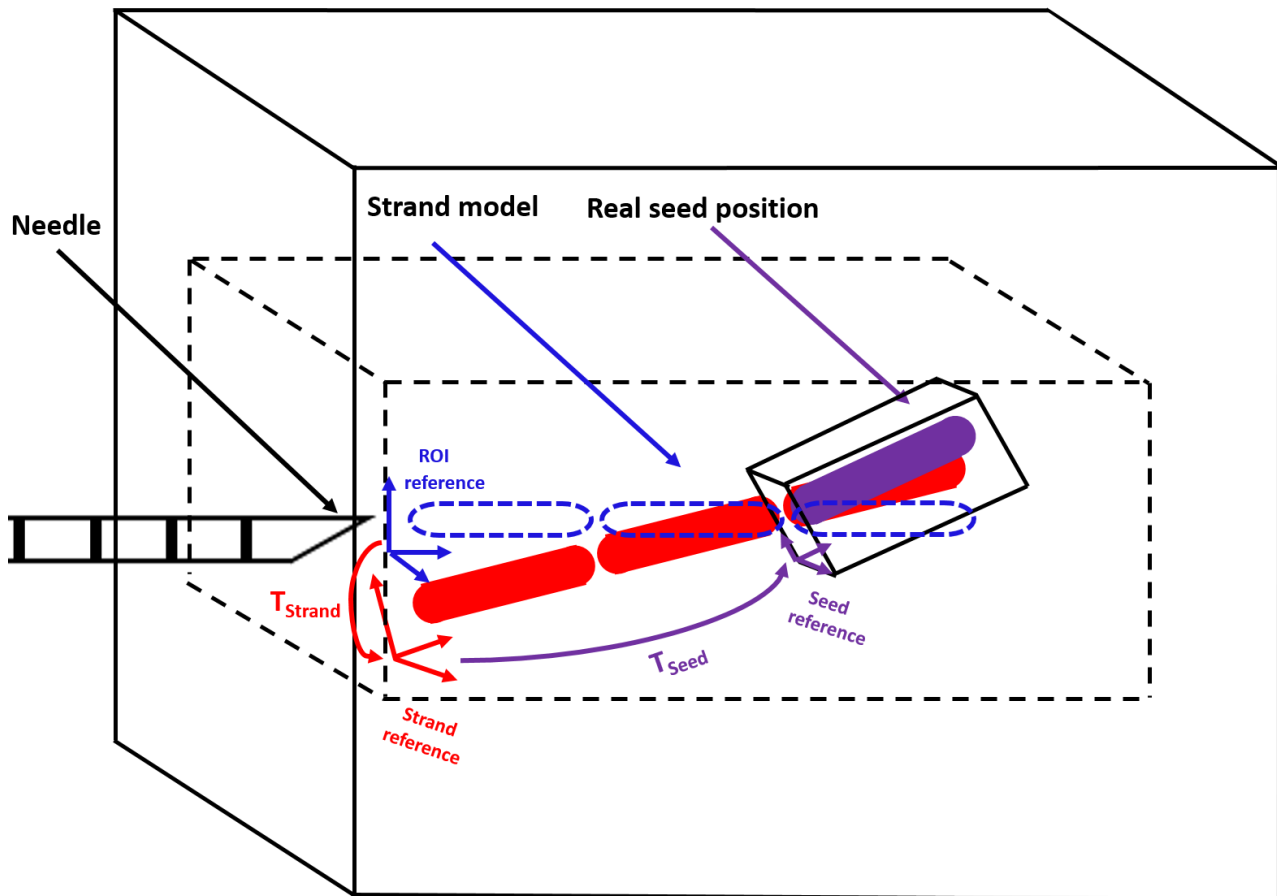


Figure 4: Reference frames and rigid transforms used by the method: global image, ROI, strand and seed references frames - positions of the strand and the individual seeds are encoded using respectively T_{Strand} and T_{Seed} .

fig:References

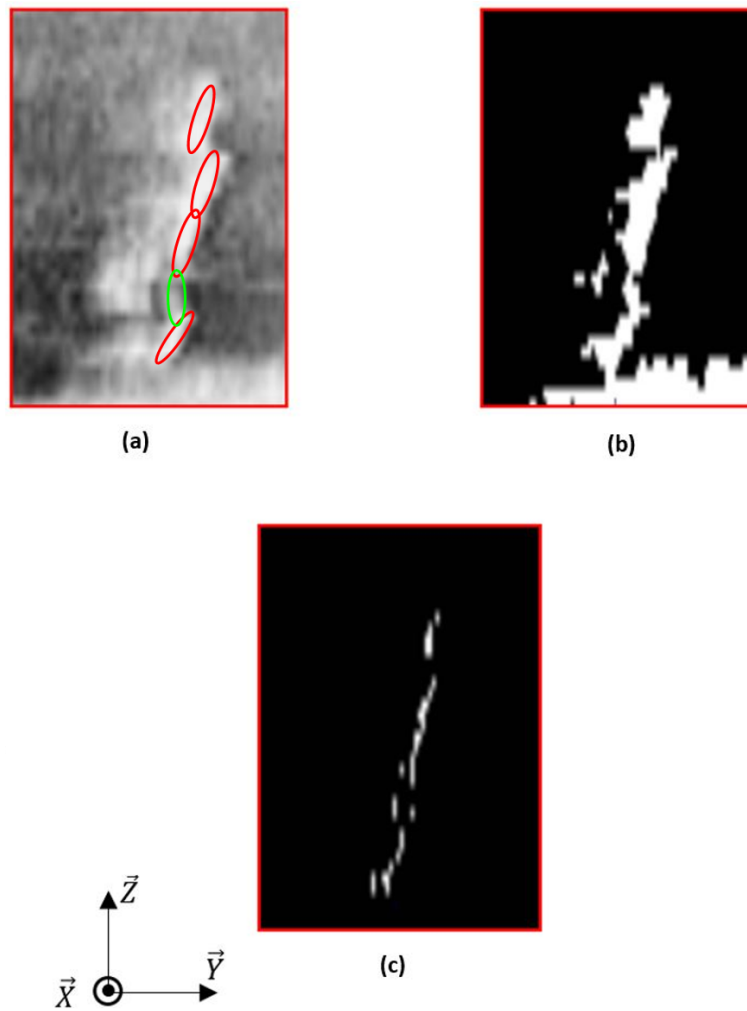


Figure 5: Sagittal sections of 3D clinical images containing stranded seeds. (a) manual segmentation based on planning information (seeds in red and spacer in green) added to the original image, (b) image after binarization with Bayesian classifier, (c) image after false positive removal with SVM classification.

fig:firstTwoSteps

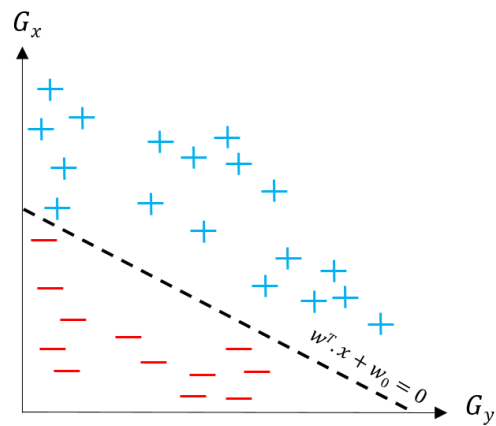


Figure 6: Example of SVM binary classification. True positives in blue and false positives in red.

fig:hyperplane

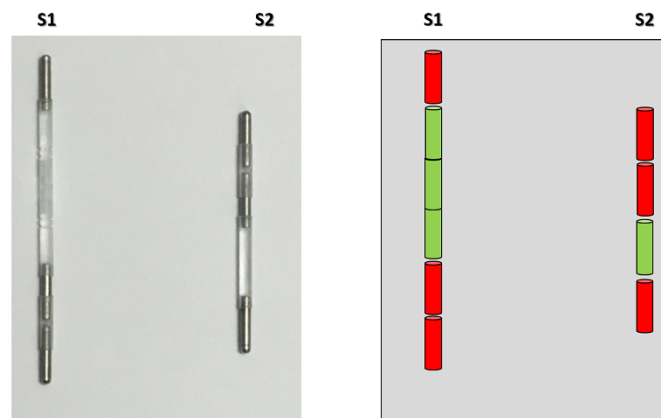


Figure 7: Two stranded seeds S1,S2 (left) with their model (right). Red cylinders represent radioactive seeds and green ones are for spacers and linkers.

fig:StrandedSeeds

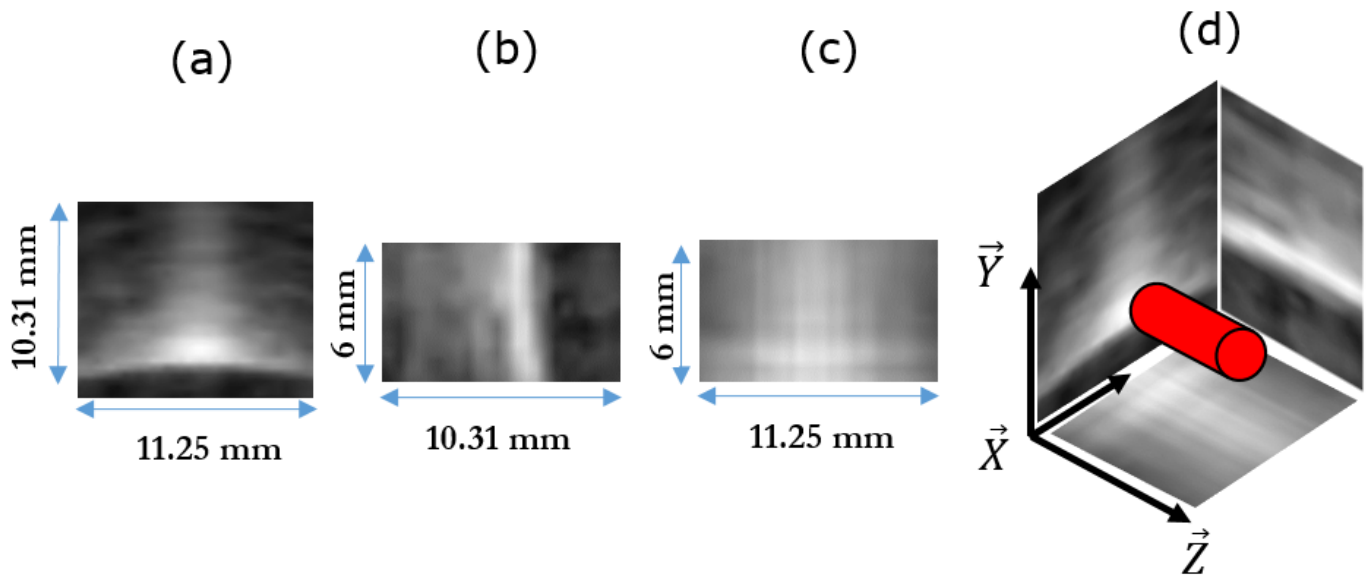


Figure 8: Artifacts in the 3 planes containing the seed in V_m of phantom image. (a) axial plane, (b) sagittal plane, (c) transversal plane. The seed visualized in (d) is perpendicular to the axial plane.

fig:VS

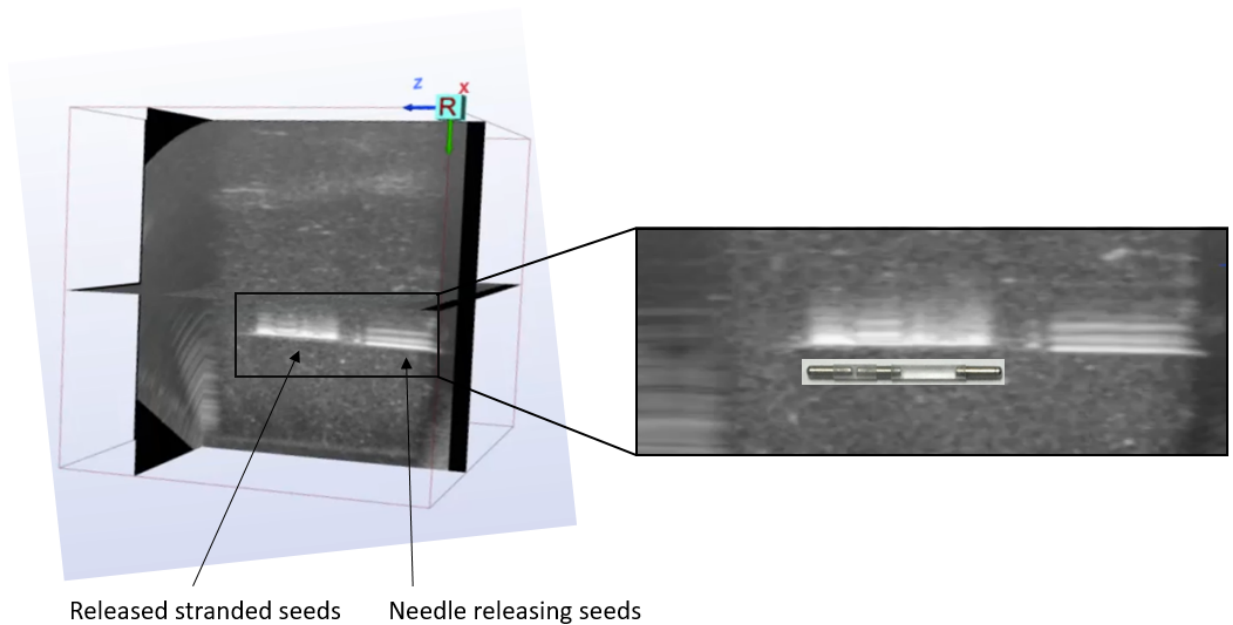


Figure 9: 3D US phantom image showing a needle during releasing stranded seeds.

fig:phantom-seed

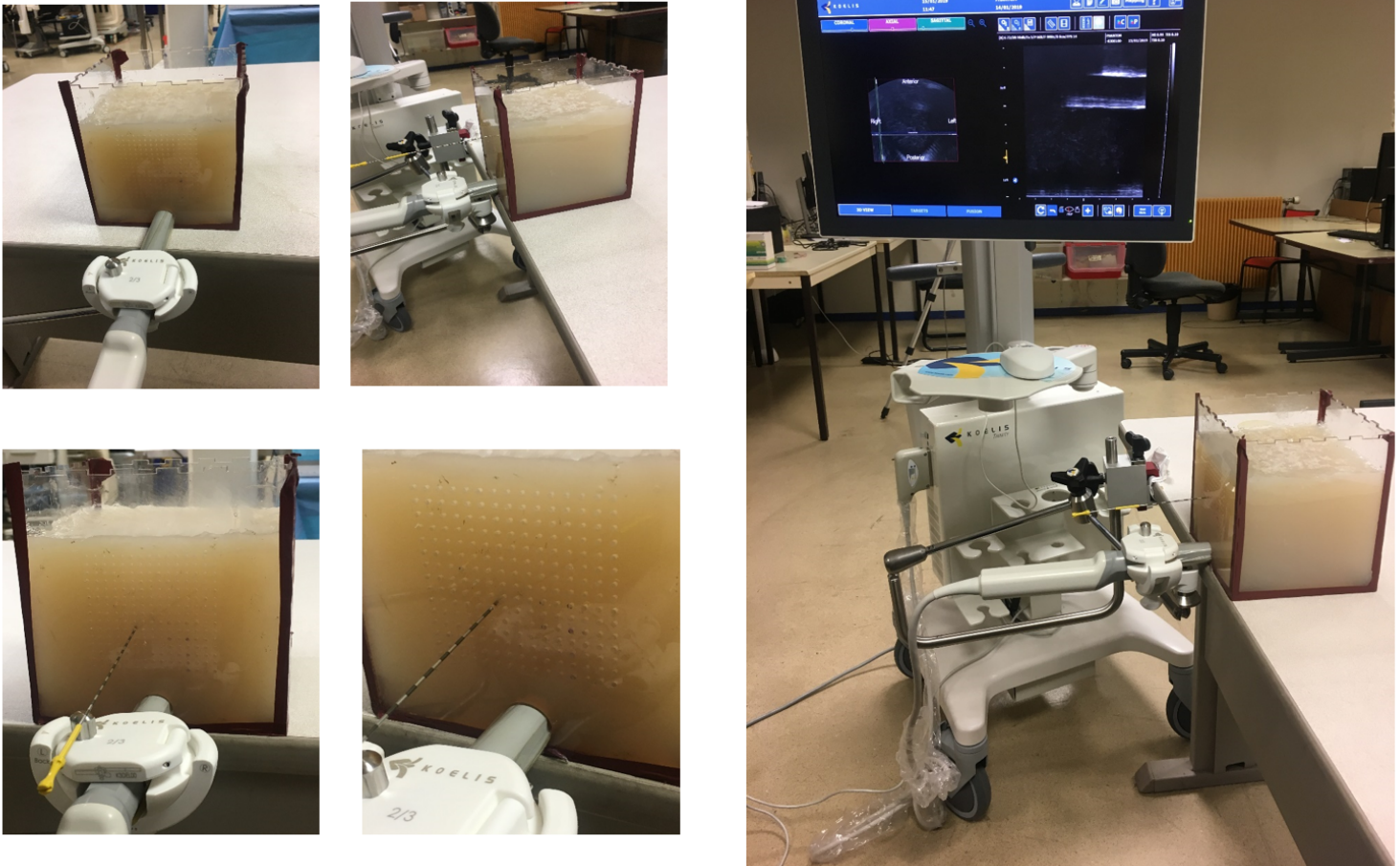


Figure 10: Experiments on Agar-agar phantom contained in a plastic box using the ultrasound probe of the TRINITY® (Koelis, Meylan, France) assistance workstation.

ity_workstation

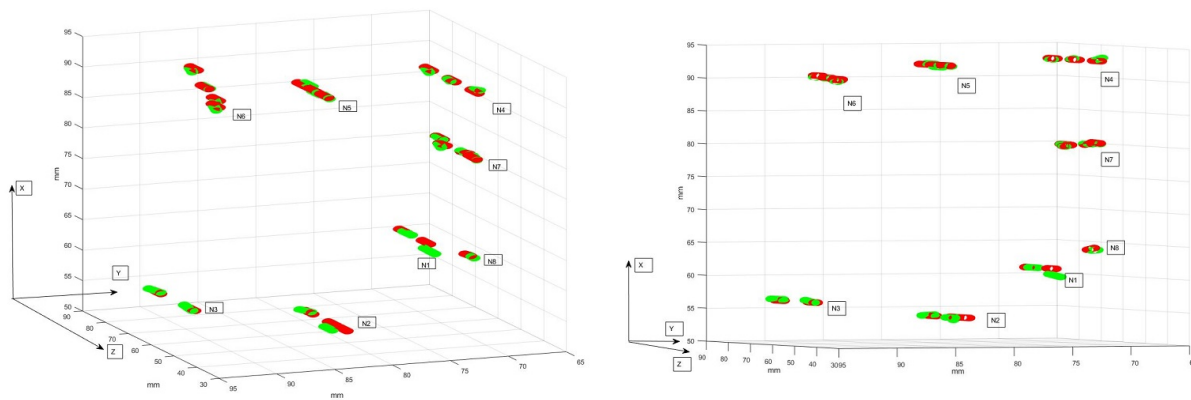


Figure 11: Seed localization result compared with manual identification ground truth at two different viewpoints. The red cylinders correspond to automatic seeds localization and the green cylinders to the ground truth. Names of the strands (cf table [2](#)) are next to them.

fig:resultUSPhantom

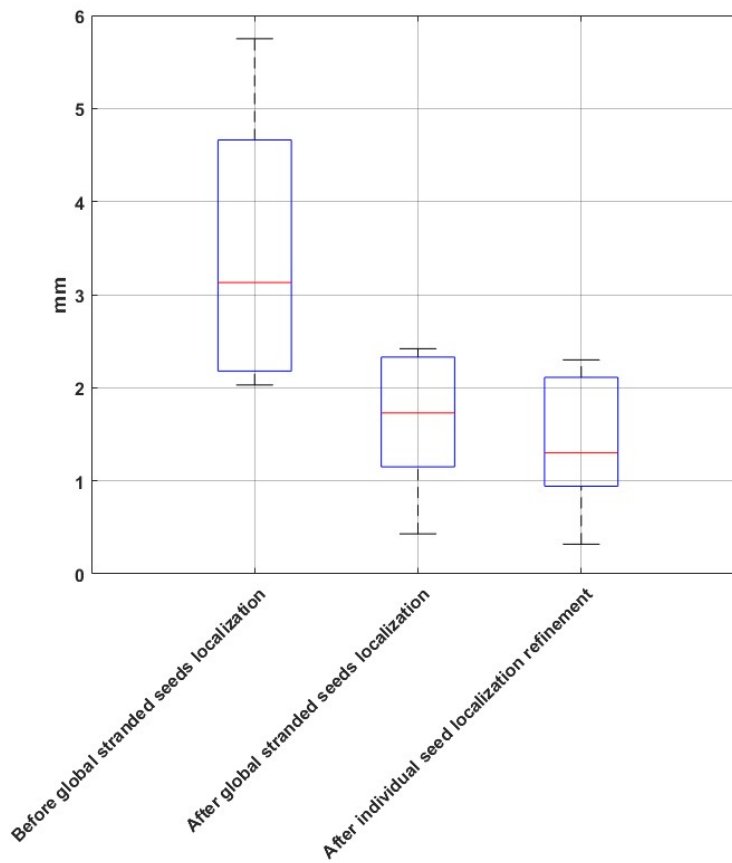


Figure 12: Boxplots presenting the distributions of the seeds localization errors in phantom images at the different stages of the method. The boxplots visualize the minimum and maximum scores (blue lower and upper dashes), the first and third quartiles (blue boxes) and median (red dash).

fig:boxplotPhantom

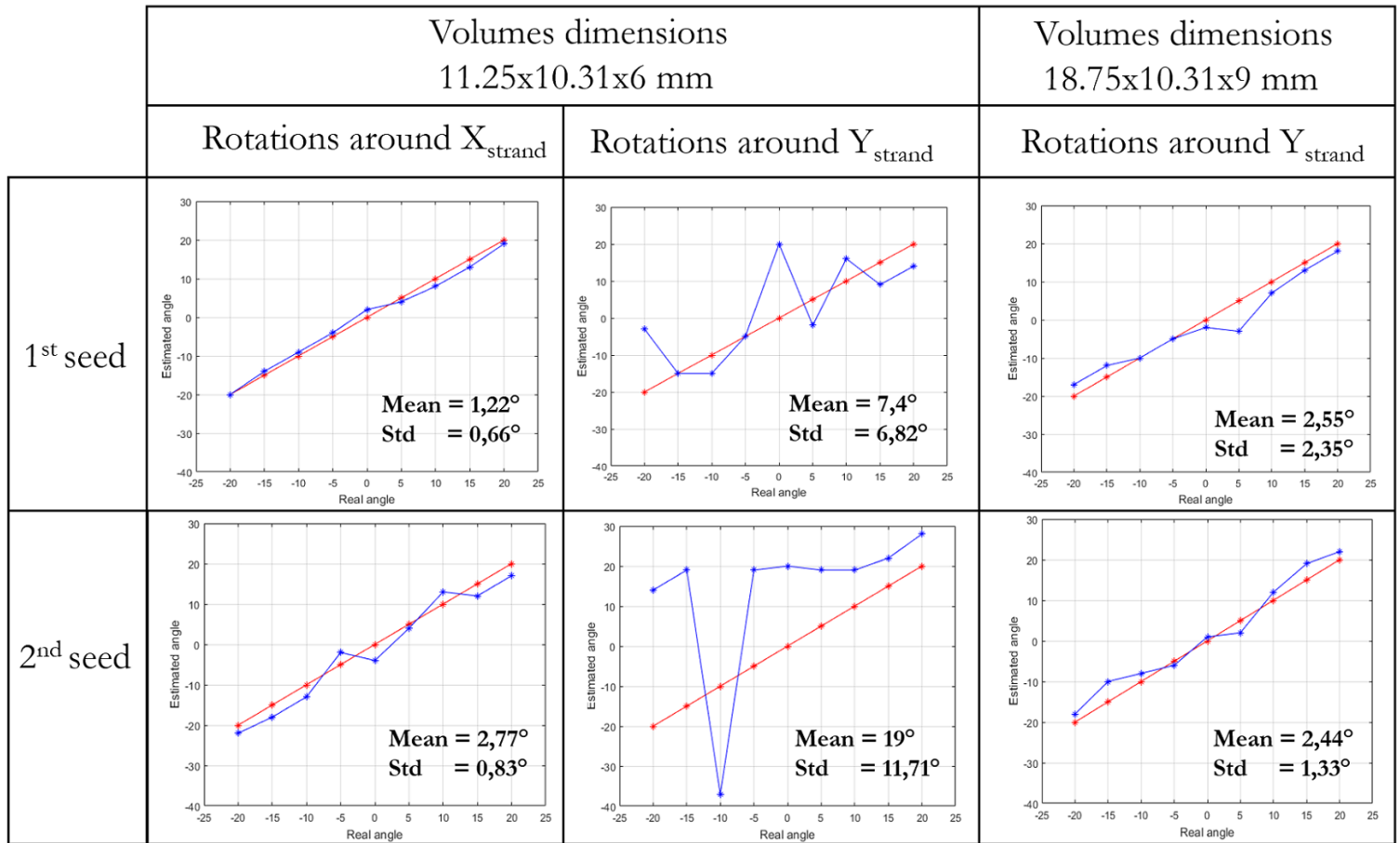


Figure 13: Estimation of the orientations of two seeds with different volumes dimensions. {Red,Blue} points are respectively the {applied,estimated} angles.

fig:orientations

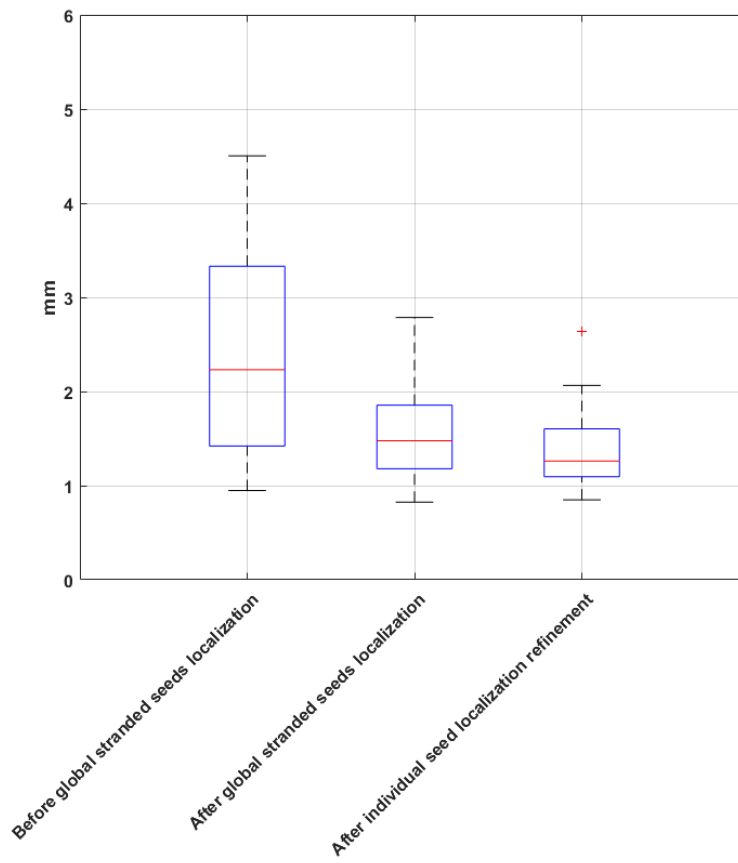


Figure 14: Boxplots presenting the distributions of the seeds localization errors in clinical images at the different stages of the method.

Lotpatients